Laser-induced incandescence (2λ and 2C) for estimating absorption efficiency of differently matured soot

Sandra Török[1] · Manu Mannazhi[1] · Per-Erik Bengtsson[1]

Abstract

Two-wavelength and two-color laser-induced incandescence (2λ–2C-LII) was used to study the absorption properties of three types of cold soot of different maturity from a mini-CAST soot generator. LII fluence curve analysis allowed for estimating absorption wavelength dependence in terms of dispersion coefficients ξ by the use of two excitation wavelengths (532 and 1064 nm). The estimated ξ (based on $E(m, \lambda) \propto \lambda^{1-\xi}$) spanned from ~ 1.2 for the mature soot, up to 2.3 for the young soot. The results for the mature soot showed good agreement with previous measurement using multi-wavelength extinction. For the young soot, however, some discrepancy was observed suggesting a weaker wavelength dependence (lower ξ) from the LII fluence analysis. Furthermore, an estimation of the $E(m, \lambda)$ for the different types of soot was done from the experimental fluence curves with temperature analysis in the low-fluence regime and simulations using an LII model. Additionally, uncertainties and limitations were discussed. Finally, it should be pointed out that caution has to be taken when interpreting 2λ-LII results to obtain quantitative absorption properties of less mature soot, which may be influenced by thermal annealing during the laser pulse and by absorption from non-refractory species externally/internally mixed with the soot.

1 Introduction

The complex nature of soot formation has been investigated for decades [1, 2]. As the first incipient soot particles are formed during combustion, they will not only grow and aggregate but also transform physicochemically depending on the chemical environment and temperature–time history [3]. The amorphous young soot of large H/C ratio will then dehydrogenate and carbonize to more ordered graphitic structures (of sp2 character). This maturation process and coupled parallel evolution of the enhanced absorption properties of soot in a combustion environment has been observed in many studies [4–9]. Soot is often considered as the second largest contributor to global warming, after carbon dioxide [10, 11], which is related to its strong absorption efficiency of radiation. Still, the uncertainty regarding the climate impact of soot due to variations in nano-structure and composition, and thereby absorption properties motivates further research on the matter.

It has been observed and described in many papers that the absorption efficiency and absorption wavelength dependence in the visible (VIS) and near-infrared region (NIR) is highly dependent on the extent of soot maturity [4–8, 12–15]. Nascent young soot absorbs more weakly due to its less ordered nano-structure, but has a much stronger absorption wavelength dependence than mature soot. The absorption efficiency of soot is often described through the dimensionless absorption function $E(m, \lambda)$, where m is the complex refractive index and λ is the wavelength. For mature soot, $E(m, \lambda)$ is generally estimated in the range of 0.32–0.4 in the VIS and NIR, as shown in the review by [16], while values as low as 0.11 ($\lambda = 1064$ nm) have been estimated for immature mini-CAST soot [17] and 0.19 at 8 mm height above burner (HAB) in a premixed $\Phi = 2.1$ ethylene–air flame [4]. Variations in soot absorption properties with wavelength are commonly described by the use of the dispersion coefficient ξ, from the relationship $E(m, \lambda) \propto \lambda^{1-\xi}$ [15]. Hence, $\xi = 1$ indicates no wavelength dependence of $E(m, \lambda)$, and previous works have shown that $\xi \approx 1$ for mature soot. In a sooting premixed McKenna flame, values as high as $\xi = 4.5$ were estimated at low HAB (by analyzing wavelengths above 685 nm), but approached 1 for increasing heights as for mature soot [8]. Similarly, high ξ was estimated by [14]. The dispersion coefficient ξ can also be termed absorption Ångström exponent, AAE. Another way to express

✉ Sandra Török
  sandra.torok@forbrf.lth.se

[1] Division of Combustion Physics, Department of Physics, Lund University, Box 118, 221 00 Lund, Sweden

the wavelength-dependent absorption is to assume that the absorption is proportional to~ $1/\lambda$, and derive the ratio between measured $E(m)$ values at different wavelengths.

For the past couple of years, different miniature combustion aerosol standard (mini-CAST) soot generators have been developed for the purpose of producing cold soot with different characteristics, with high stability and repeatability [18, 19]. Previous studies have shown that the mini-CAST can produce soot particles with great variety in composition, nano-structure, and optical properties, from small young particles with high organic carbon fraction and strong absorption wavelength dependence, to differently sized mature aggregated particles with low organic carbon fraction and with an absorption function $E(m)$ independent of wavelength [12, 17–25]. As it is of great interest, for calibration and legislation purposes, to find laboratory soot sources producing soot with properties resembling those of real sources, the resemblance of mini-CAST soot with soot from diesel engines and aircraft turbines has been studied [19–22, 26].

One of the most common tools used for qualitative and quantitative measurements of soot in different environments is laser-induced incandescence (LII) [15, 27]. The technique has been utilized (in imaging or time-resolved mode) to measure soot concentrations and particle sizes in combustion and ambient environments, see, e.g., [15], but also to study the absorption properties of soot using two excitation wavelengths [5, 6, 14, 28, 29]. In this work, we have studied the absorption properties of three different types of cold soot of different maturity from a mini-CAST soot generator using LII in a setup using two excitation wavelengths (2λ) and two detection colors (2C). This combination allows for studying both the absorption wavelength dependence, the absorption efficiency, and the wavelength-dependent emission properties of the different types of soot. Specifically, we have studied the fluence curves of the different types of soot, for example using the method described in [14] to estimate the LII dispersion coefficient, but we also estimate the laser-induced fluorescence contribution to the measured signals when using an excitation wavelength in the visible wavelength range. Furthermore, we study the temperature evolution of laser-heated soot to estimate $E(m, \lambda)$ for the mini-CAST soot. Finally, we specifically focus our discussion on the feasibility of applying the presented method on young soot and discuss limitations and uncertainties in our estimations.

2 Laser-induced incandescence

In laser-induced incandescence (LII), an intense laser pulse heats the strongly absorbing soot particles (with properties close to a black-body) to high temperatures (3000–4000 K)

[15, 27]. When reaching these high temperatures, the soot Planck radiation, which is the LII signal, will to large extent be distributed in the visible spectral range, allowing detection spatially, spectrally, and/or temporally. The main cooling mechanisms for the heated soot are sublimation and heat conduction, which at high temperatures will limit continuous temperature increase during the laser pulse, as both the heat conduction and level of sublimation depend on the temperature of the soot [15].

The peak intensity in the time-resolved LII signal of soot is commonly studied as a function of the laser fluence (J/cm²). Examples of such fluence curves from the present work are later shown in Fig. 2. The strong temperature dependence (T^5) of the LII signal will result in a strong signal increase for increasing fluences in the first part of the fluence curve, where absorption of laser radiation is the dominating heat transfer process. The peak LII signal will be reached during the laser pulse, and the peak LII intensity will be roughly independent of the laser pulse length on these short time scales [30]. The rate of absorption $\dot{q}_{abs}$ can be expressed, as shown in Eq. (1), where d_{pp} is the primary particle size, F_{laser} is the laser fluence, λ is the laser wavelength, and $E(m)$ is the absorption function

$$\dot{q}_{abs} = \frac{\pi^2 d_{pp}^3 E(m)}{\lambda} F_{laser}. \tag{1}$$

The change of internal energy ΔU_{int} for a soot particle which has been heated ΔT, assuming constant volumetric heat capacity for the soot in the temperature range, will be given by Eq. (2):

$$\Delta U_{int} = \frac{\pi}{6} d_{pp}^3 \rho c_p \Delta T. \tag{2}$$

Hence, investigating the temperature evolution in an absorption dominated regime and with a known volumetric heat capacity (i.e., the product ρc_p), information about the absorption properties in terms of the $E(m)$ of soot can be provided [30, 31] according to Eq. (3), where the rate of heating as a function of fluence is expressed as $\Delta T/\Delta F_{laser}$

$$E(m) \approx \frac{\lambda \rho c_p}{6\pi} \frac{\Delta T}{\Delta F_{laser}}. \tag{3}$$

The soot starts to sublime when heated to temperatures around 3400 K [4] and higher, which corresponds well with the inflexion point in the fluence curves. The sublimation will, along with an increasing heat conduction loss, make the signal reach a maximum for increasing fluences, after which it starts to decrease mainly due to extensive mass loss.

Fluence curves have historically been of great interest, generally in the pursuit of finding a fluence-independent LII signal region in quantitative 2D soot imaging measurements, or for establishing suitable fluence below the sublimation

threshold in low-fluence LII for particle sizing [32]. The past years however, the use of the fluence curves have become important when studying the absorption wavelength dependence by two-excitation wavelength LII (2λ-LII) and to extract information about the maturity of soot [5, 6, 14, 29]. This specific method will be implemented in this investigation.

A common tool used alongside experimental LII data is the LII model, a heat and mass transfer model, which describes the physical processes occurring during light–matter interaction, between, e.g., a short laser pulse and soot. The LII model can be used to reproduce experimental time-resolved data, commonly done to estimate soot primary particle sizes [15]. In this work, however, this model will specifically be used to retrieve information about the absorption properties of soot investigated by fitting modeled fluence curves to experimentally retrieved ones. The model developed in Lund is the one described in [33], and compared to other (at the time existing) LII models in [34].

3 Experimental setup

The LII setup used for this work, shown in Fig. 1, is based on previous setups used by our group, see, e.g., [4]. A pulsed Brilliant B Nd:YAG laser with pulse length of 6.8 ns and 10 Hz repetition rate was used at its fundamental and second harmonic wavelength of 1064 and 532 nm, respectively. The pulse energy was adjusted by an attenuator, consisting of two thin-film polarizers and a quarter wave-plate, to keep the same pulse characteristics for all measurements. A circular aperture was used to cut out the center 4 mm part of the beam to achieve a top-hat profile, for homogeneous heating of soot within the probe volume. The cut-out center part of the beam was relay imaged by a lens system to reach
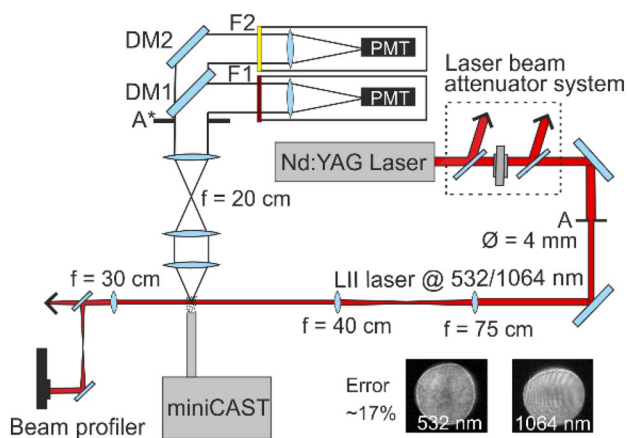

Fig. 1 The experimental setup used for the 2C–2λ-LII measurements. Beam spatial profiles are shown for both 532 and 1064 nm. *A* aperture (*-adjustable), *DM* dichroic mirror, *F* band-pass filter (1–684 nm, 2–575 nm)

a diameter of 2 mm in the probe volume. A beam profiler camera was used to monitor the top-hat spatial profile, which is shown in the setup schematics (Fig. 1). A broad-band calibration lamp (Labsphere 1000) was used for temperature calibration by pyrometry.

On the detection side, three achromatic doublets were used to collect and collimate the LII signal. Two dichroic mirrors were then used to separate the signal and two band-pass filters were used to select the wavelengths of interest (575 and 684 nm with 25 and 24 nm bandwidth, respectively). Two Hamamatsu H10721-20 photomultiplier tubes were used for signal detection.

The soot generator, a mini-CAST 5201c [35], operated with propane (C_3H_8) as fuel, was used and run at different operation points (OP) to generate three types of polydisperse soot (OP1, OP6, and OP7), which previously have been characterized by our group. In [12], the investigation of the optical properties (using in-situ multi-wavelength extinction) and particle composition showed that the particles span from poorly absorbing young soot with a high organic carbon content (87%; OP7 soot), to strongly absorbing mature soot with only a minor fraction of organic content (OP1 soot). Furthermore, in [36], the observed variations in laser-vaporized carbon fragment mass spectra using a Soot Particle Aerosol Mass Spectrometer (SP-AMS) and the differences in the soot nano-structure obtained by high-resolution transmission electron microscopy (HR-TEM) image analysis were related to the composition and maturity of soot. Additionally, in [25], the internal bonding structure of mini-CAST soot was characterized by Raman spectroscopy. The settings for the different OP cases and the operational principle of the soot generator have been described in more detail in [12].

4 Results and discussion

4.1 Observations of absorption efficiency

The normalized fluence curves at two detection wavelengths (575 and 684 nm) for all studied types of soot (OP1, OP6, and OP7) using two excitation (532 and 1064 nm) wavelengths are presented in Fig. 2a, b. The data presented are the peak LII signal intensity averaged over a 4 ns interval around the time-resolved maximum as a function of fluence, where each data point is averaged from 300 single shots. In Fig. 2a, a large difference between the curves for $\lambda_{\text{excitation}} = 1064$ nm is shown, where much higher laser fluence is needed to heat the most immature soot particles (OP6 and OP7) to their maximum LII temperature, in comparison with the more mature particles (OP1). It is suggest that the observed differences are mainly related to differences in the absorption efficiency for different soot types, which has also been observed in many other works during maturation in
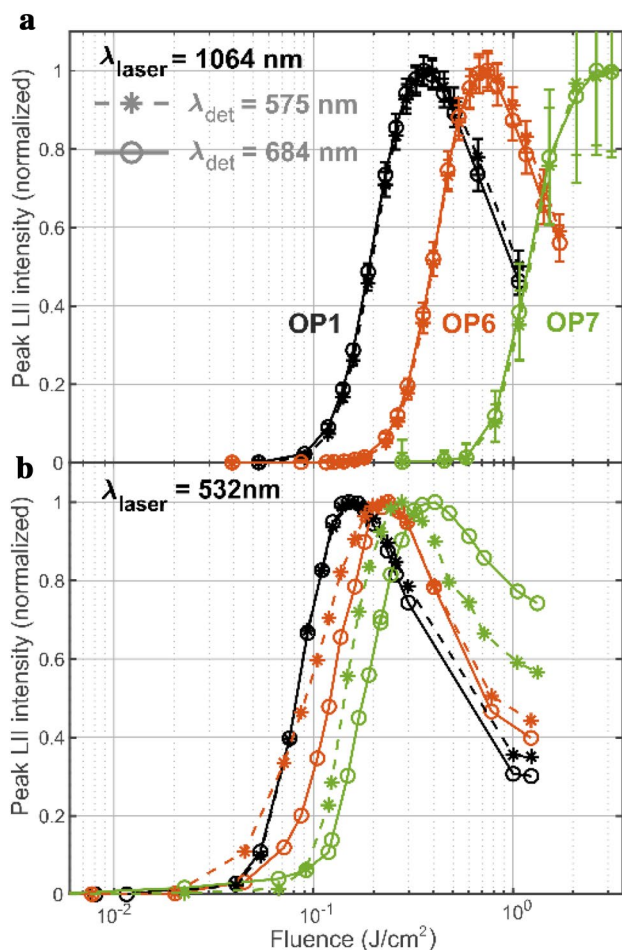
Fig. 2 The normalized fluence curves are shown for three types of soot (denoted OP1, OP6, and OP7) using the excitation wavelengths of **a** $\lambda_{\text{excitation}} = 1064$ nm and **b** $\lambda_{\text{excitation}} = 532$ nm, where solid lines show the results using $\lambda_{\text{detection}} = 684$ nm and dashed lines $\lambda_{\text{detection}} = 575$ nm. The relative shift of the fluence curves indicates the absorption efficiency for the different types of soot at the given wavelength. For excitation at 532 nm, a clear signal contribution from LIF can be observed for OP6 and OP7 as the curves are shifted with detection wavelength. Note the logarithmic scale for the x-axis to more easily display the difference between the curves. The data spread (1 std) is only shown in figure **a**, to keep figure **b** easier to read. The spread is approximately the same independent of laser wavelength

flames [4–6, 9, 14, 37, 38]. It should however be noted that direct comparison between the curves is not straightforward as the soot for the different OP cases have different characteristics, as discussed later in this section.

For $\lambda_{\text{excitation}} = 532$ nm presented in Fig. 2b, we observe that the fluence curves have been shifted to lower fluence in comparison with excitation at 1064 nm, but also that the curves for OP6 and OP7 soot have been shifted relatively more compared to the one for OP1 soot. When observing the solid lines, showing the LII signal at detection wavelength 684 nm, it can be seen that the curves have similar

appearance as for the previous case in Fig. 2a, but for the detection wavelength of 575 nm, shown as dashed lines, the curves for OP6 and OP7 soot are even more shifted and even partly overlap with the OP1 fluence curve. The reason for this behavior is that the measured LII signal is contaminated with laser-induced fluorescence (LIF), possibly from the immature soot itself, from condensed polycyclic aromatic hydrocarbons (PAHs), and other volatiles in the freshly emitted soot particles [12, 39]. We hence observe that the LIF contribution to the LII signal depends strongly on the detection wavelength.

4.2 Analysis of dispersion coefficients

As the shift in the LII fluence curves for mini-CAST soot was related to different degrees of soot maturity, we further investigated how the relative shift for each type of soot depends on the excitation wavelength. The methodology first presented by [28] was used, where the fluence curves are scaled to overlap to retrieve the wavelength dependence of the soot absorption properties for a certain type of soot. This method is valid if the wavelength dependence of the absorption cross section is the only parameter influencing the energy needed to reach the peak LII signal for each type of soot. Hence, PAH interference is avoided in the evaluation by overlapping fluence curves obtained from the delayed LII signals at around 50 ns after peak LII signal [6, 14, 29], see section S1 in supplemental information. The dispersion coefficient ξ can now be derived as it is related to the used wavelengths (532 and 1064 nm) and fluences F_{532} and F_{1064} that give rise to the same amount of energy absorbed by the soot and hence, the same LII signal, according to Eq. (4):

$$\xi = \frac{\log\left(\frac{F_{532}}{F_{1064}}\right)}{\log\left(\frac{532}{1064}\right)}. \tag{4}$$

The dispersion coefficient ξ, which is also often termed as the absorption Ångström exponent (AAE) [40] in the aerosol community, describes the absorption wavelength dependence in a given wavelength range. In Fig. 3, the evaluated dispersion coefficients ξ_{LII} of the three types of soot investigated are shown and compared to those previously evaluated from multi-wavelength extinction measurements [12]. For the more mature OP1 soot, the dispersion coefficient shows values close to 1, while the less mature soot shows higher values in agreement with previous investigations, see, e.g., [7, 11, 14]. Hence, a clear trend is obtained, where the dispersion coefficient reflects the relative level of maturity. The multi-λ extinction results shown are dispersion coefficients obtained using wavelengths above 650 nm ($\xi_{\text{ext}\_\lambda \geq 650\,\text{nm}}$), and measurements done on the soot after being heated to 800 K ($\xi_{\text{ext\_Oven}}$; $\lambda = 405–1064$ nm).
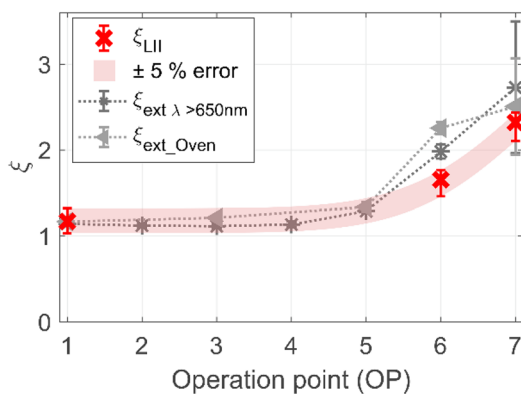
Fig. 3 The dispersion coefficients ξ for soot produced at three different operating conditions are shown; OP1, OP6, and OP7. ξ_{LII} is close to 1 for the most mature soot, while for the younger soot, the values become higher, indicating stronger wavelength-dependent absorption. Results from multi-λ extinction measurements are inserted for comparison from [12]. $\xi_{ext\lambda>650\ nm}$ shows results when evaluated using wavelengths of 650–1064 nm, ξ_{ext_Oven} show results evaluated from mini-CAST soot with thermal treatment to 800 K using wavelengths 405–1064 nm. The shaded area shows an estimated error of $\pm 5\%$ of the absolute fluence value (a high-order polynomial was used to obtain the smooth curve)

Fig. 4 The temporal LII signal for OP1, OP6, and OP7 soot shown for maximum LII signal intensities using 1064 nm. The curves are normalized to allow for comparison and a clear difference in decay time can be observed. A minor bump right after peak can be observed, which is due to the PMT response to a rapid signal increase (< 10 ns)

The agreement between LII-derived and multi-wavelength-extinction-derived dispersion coefficients is good for the most mature OP1 soot. For the less mature soot presented in Fig. 3, with high organic fractions, a discrepancy is observed for OP6 soot as the dispersion coefficient is lower from the LII-derived ξ in comparison with the multi-wavelength extinction measurements. For OP7, the results appear to agree well; however, due to the relatively short time-resolved LII signal, quite large uncertainty can be assumed due to poor signal-to-noise ratio. In Fig. 4, the temporal LII signal is shown for the different types of soot, and it is clear that for OP7 soot, the signal is very low at 50 ns after peak LII.

Both sets of extinction-based measurements included in Fig. 3 show the dispersion coefficient of the refractory soot itself by avoiding absorption by PAHs and other volatile organics, as the vast majority of such volatile species have evaporated after heating to 800 K [12], and additionally, they absorb poorly at wavelengths above 650 nm hence having negligible influence on the estimated ξ [39]. To explain this discrepancy, we speculate on the potential influence of thermal annealing [15, 41] during the laser pulse, which would enhance the soot absorption efficiency and lead to a lowering of the dispersion coefficient. It should be noted here that multi-wavelength extinction measures the absorption directly at room temperature, while the LII measures the absorption indirectly over a large temperature span from room temperature to temperatures up to approximately 4000 K. In previous studies, enhanced absorption has been
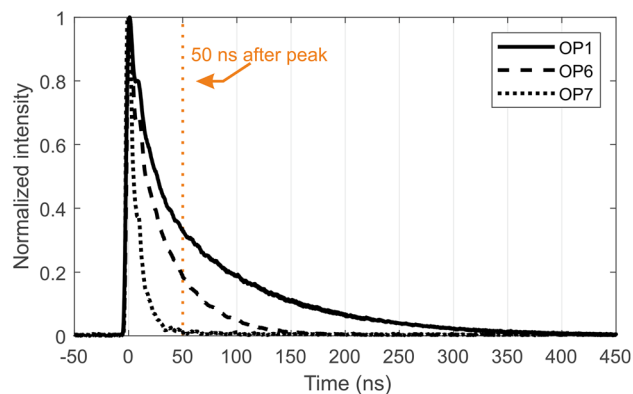
observed as a result of pre-heating the soot with another laser pulse [41–43]. In [43, 44], the extinction through a soot-laden probe volume was monitored when exposed to pulsed laser heating. A rapid increase of the extinction was observed during the laser pulse, assigned to the possible annealing process of soot and hence enhanced absorption. On the contrary, Migliorini et al. observed an increasing dispersion coefficient when laser-heating ethylene soot prior to extinction measurements [45]. The reason for this might however be due to the observed generation of newly formed particles from the vaporized carbon fragments, which may contribute to absorption at the shorter wavelengths (below ~ 700 nm) possibly due to its small size [46] and/or less mature character [47]. For our experiments, it is not made clear at which time frame annealing (influencing the absorption efficiency) occurs, and the restructuring of the nano-structure itself might range beyond the time of the heating laser pulse.

4.3 Laser-induced fluorescence (LIF) interference

In Fig. 2b, we observed the influence of laser-induced fluorescence (LIF) on the fluence curves obtained using the excitation laser of 532 nm, and it appeared that the fluence curves depended strongly on detection wavelength. In Fig. 5, we show the fluence curves of each type of soot scaled according to the normalization point at 50 ns after the peak LII signal, which was used for analysis of dispersion coefficient in the previous section. Hence, we can quantify the LIF contribution to the fluence curves when using the 532 nm excitation wavelength. The fluence curve of 1064 nm excitation wavelength shown in black lines shows the LII signal from the black-body radiation of the soot,
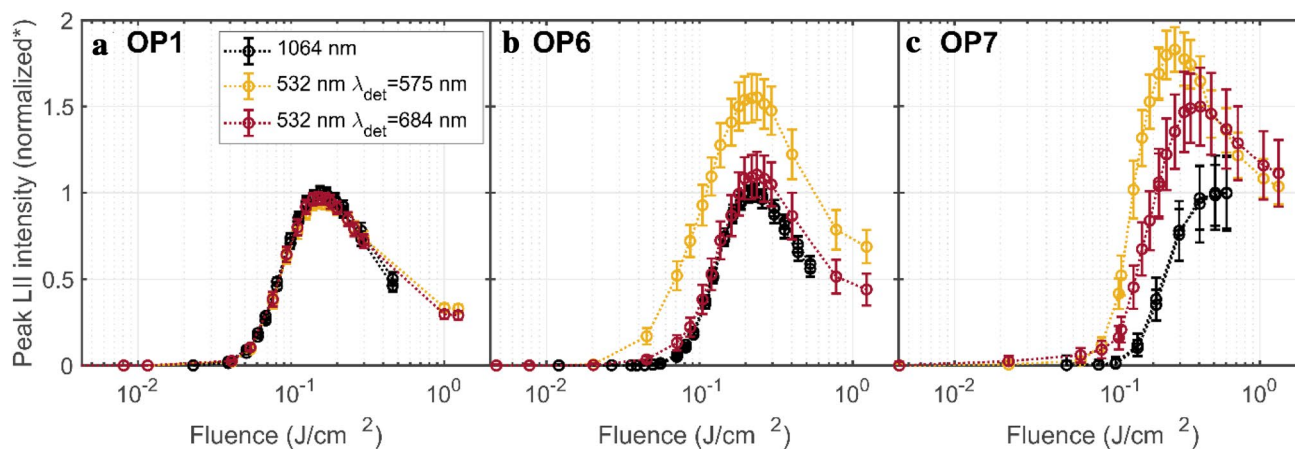
Fig. 5 The contribution of LIF is shown for the three different types of soot, specifically **a** OP1, **b** OP6, and **c** OP7. The LIF contribution is negligible when using an excitation wavelength of 1064 nm, and hence, this case is considered as pure LII signal (black lines), while the excitation wavelength at 532 nm induces LIF and different inten-sities are detected depending on detection wavelength. The fluence curves are shifted according to the normalized fluence curves at 50 ns delay in both *x*- and *y*-axis, see section S1 in supplemental information. (The error bars show 1 std.)

while the yellow and red lines show the LII + LIF fluence curves at the two detection wavelengths (from excitation wavelength of 532 nm). As expected, since OP1 soot has very low organic fraction, no significant LIF was observed for OP1 (Fig. 5a). For OP6, however, the LIF signal is prominent. As can be expected when using an excitation wavelength of 532 nm, the LIF signal contribution is highest at 575 nm [39], but still a substantial LIF contribution is also observed at 684 nm. For the OP6 soot, the LIF contribution at 684 nm is about one-fifth of the contribution at 575 nm, which is in the range of what has been observed in diffusion flames burning on diesel [39]. An example of the temporal signal with LIF contribution can be seen in Figure S2 in the supplemental material. For OP7, we observe a similar trend as for OP6; however, it should be mentioned that the short signal of OP7 soot (displayed in Fig. 4) resulted in that the estimated LIF contribution to the signal is very sensitive to the choice of delay-time. Hence, the results in Fig. 5c have higher error bars.

4.4 *E*(*m, λ*) estimations

To enable quantification of the absorption properties of the mini-CAST soot in our study, we investigated the temperature evolution in the absorption dominated fluence curve regime (low-fluence regime) where the soot is heated to LII temperatures, but sublimation is not a dominant loss term (< 3400 K [4]), see the temperature curve in Fig. 6a. As described in Sect. 2, the *E*(*m, λ*) can be estimated using Eq. (3), given that the temperature evolution at the sublimation-free regime is studied [31]. A linear fit is performed in the region where the LII signal is high enough for good S/N ratio and where there is no substantial sublimation (below

3400 K). The fit is shown in Fig. 6a and results in an *E*(*m*, 1064 nm) of 0.33 (using $\rho c_p = 4.6$ J/cm^{3}K [48]) for OP1 soot, which agrees well with values presented in the literature, where generally *E*(*m, λ*) = 0.32–0.4 is considered valid for mature soot in the VIS and NIR region [16]. The result also agrees well with estimations based on extinction measurements of similar soot, CAST1, from the same type of Mini-CAST (*E*(*m*, 1064 nm) = 0.32) studied in [17].

The LII model was not used for estimations of *E*(*m*, 1064 nm) directly as it is known to have difficulties in reproducing the influence from sublimation and as it allows superheating [4, 49], nevertheless, it was used for estimations of *E*(*m*, 1064 nm) for OP6 and OP7 soot based on the estimated value for OP1. The modeled results shown in Fig. 6b are done on single primary particles of the estimated mean size obtained from TEM image analysis (presented in Table S1 in the supplemental information). The estimated *E*(*m*, 1064 nm)$_{model}$ for the mini-CAST soot types are shown in Table 1. The trend shows that more mature soot has a larger *E*(*m*, 1064 nm) indicating a higher absorption efficiency than the less mature soot, as expected. In Fig. 6b, experimental fluence curves are presented for OP6 and OP7, along with modeled curves. For OP6 and OP7 soot *E*(*m*, 1064 nm) values are estimated as low as 0.16 and 0.05, respectively. Similar results were obtained by Bescond et al. [17], who evaluated an *E*(*m*, 1064 nm) of 0.11 for young mini-CAST soot with a OC/TC ratio of 87%, which roughly corresponds to the (OC + PC)/TC ratio of our OP7 soot.

The derivation of LII temperature of the OP1 soot was done assuming black-body radiation [4], and the *E*(*m, λ*) ratio based on the estimated dispersion coefficient of OP1 soot. Resulting temperatures which depend largely on the experimental conditions seem to agree well with
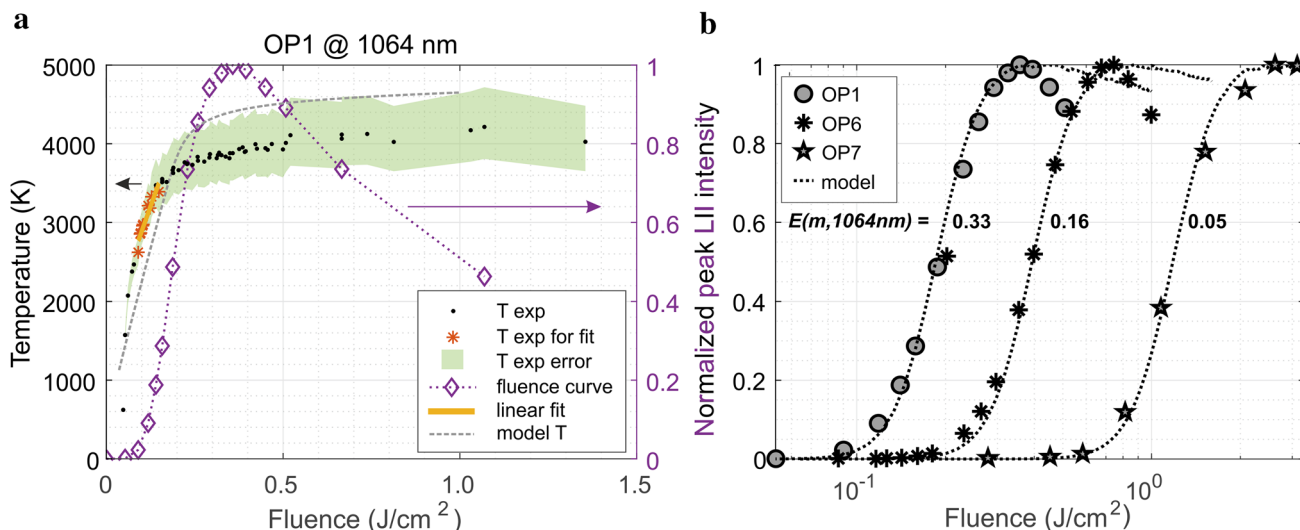
Fig. 6 In **a,** the black dots show the temperature evolution as a function of fluence for OP1 soot. The number of data points are more than for the fluence curve, as data from the repeated measurements were included to increase the accuracy of the analysis. In the low-fluence regime, a linear fit is performed along the red stars to obtain the linear temperature increase (shown as a yellow line) for $E(m, 1064\text{ nm})$ estimations. The green area shows a $\pm 5\%$ error (corresponding to the approximate uncertainty originating from the LII signal ratio).

The corresponding LII fluence curve is shown for comparison. In **b,** the experimental fluence curves for OP1, OP6, and OP7 soot using $\lambda_{\text{excitation}} = 1064$ nm, $\lambda_{\text{detection}} = 687$ nm, are shown together with the fitted fluence curves using the Lund LII model. The $E(m, 1064\text{ nm})$ used for best agreement of OP6 and OP7soot was 0.16 and 0.05, respectively. The trend shows decreasing $E(m, \lambda)$ when moving towards operating points producing more immature soot

Table 1 The estimations of the absorption function $E(m, \lambda)$ for the three types of soot

Mini-CAST soot	$E(m, 1064$ nm) from low-fluence regime and model	$E(m, 532$ nm) from ξ
OP1	0.33	0.37
OP6	0.16	0.25
OP7	0.05	0.12

The $E(m)$ at 1064 nm is based on the temperature trend in the low-fluence regime for OP1 at 1064 nm and on LII model for OP6 and OP7, while the $E(m)$ at 532 nm is estimated based on the dispersion coefficient ξ (shown in Sect. 4.2)

for example [38], where the experimental conditions were comparable. For comparison, the modeled temperature evolution is included for the OP1 soot, along with the temperature measurements in Fig. 5a. The disagreement between experimental and modeled LII temperatures at high fluence may be explained by the difficulty of the LII model to reproduce a more rapid sublimation rate as observed in experiments, and due to super-heating, as previously discussed [4, 49]. The discrepancy at low fluence may be related to, e.g., shielding effects [50] which are not taken into account in our simulations, or due to the non-even top-hat profile which would allow the fraction of soot at higher T to be more dominant due to the T^5-dependence of the LII signal.

The dispersion coefficient ξ shown in Fig. 3 is further used to estimate $E(m, 532$ nm) for the studied soot. By extrapolating from the estimated $E(m, 1064$ nm), this can be retrieved using Eq. (5):

$$E(m, 532\text{nm})_{\xi} = E(m, 1064\text{nm}) \cdot \left(\frac{532\text{nm}}{1064\text{nm}}\right)^{1-\xi}. \quad (5)$$

The resulting $E(m, 532$ nm)$_{\xi}$ is presented in Table 1 for the different OP cases. It can be concluded that the higher OP cases shows much lower absorption efficiency also at an excitation wavelength of 532 nm, although higher than at 1064 nm.

4.5 Uncertainty analysis

As the estimations of $E(m, \lambda)$ for the less mature soot types are obtained using material parameters for mature soot, we test how varying these parameters affect the resulting fluence curves and hence the $E(m, 1064$ nm) estimation for OP6 and OP7. Also, we consider the influence from the experimental conditions and the simplifications done to reproduce the fluence curves retrieved experimentally. Apart from the assumptions made in the LII model, we will also consider measurement errors to highlight important aspects when considering fluence curves from young soot with substantial amount of volatile compounds.

To evaluate the influence of material parameters, fluence curves are generated using the LII model with material properties more resembling estimated values for immature soot. In the supplemental information, section S3, the full analysis is described as the primary particle size d_{pp} (10–20 nm), the thermal accommodation coefficient ($\alpha = 0.1$–0.9), and the sublimation efficiency ($\beta = 0.2$–0.9) have been varied in the $E(m, \lambda)$ estimations. From the analysis (specified in the supplemental information section S3), the effects of the adjusted material parameters were too small to influence the $E(m, \lambda)$ estimations significantly. The volumetric heat capacity (i.e., the product of the density and the heat capacity) was not varied, as in the work by Michelsen [48], a thorough analysis of the dependency on temperature and soot maturity was presented, showing convincingly that there is only minor influence related to soot maturity. Nevertheless, an uncertainty of 5% is assumed, which would translate into a 5% uncertainty of the estimated $E(m, \lambda)$.

It is well known that for soot particles exposed to high laser energy, emissions from thermally excited C_2 can be a source of error during LII measurements [15, 51–53]. The C_2 Swan band emission interference may become significant for increasing fluences above 0.5 J/cm^2 (at 1064 nm) for mature soot. However, the C_2 interference is estimated to be a minor problem as the focus in our analysis of $E(m, \lambda)$ estimations is on the low-fluence part of the fluence curve.

We previously speculated on the influence of thermal annealing on our measurements as the soot particles reach graphitization temperatures at the nanosecond scale. It is however not clear how much transformation happens during the measurements as the short time scale might limit the extent of material transformation, as pointed out in [54] for carbon blacks. Nevertheless, annealing might to some extent enhance the level of crystallinity in the soot material and hence its level of maturity and thereby its absorption wavelength dependence ξ. The exothermic nature of the annealing process and thereby its influence on the soot temperature in combination with the absorption enhancement might also be contributing to the discrepancy between measured and modeled temperature at low fluences (see Fig. 6a).

The composition of the soot in this study (OP1, OP6, and OP7) has previously been investigated in [12, 24, 25]. For OP6 and OP7 soot, extensive amount of PAH and organic carbon was part of the soot emitted from the mini-CAST generator. For example, about 20 and 74% mass fraction for OP6 and OP7, respectively, was possible to remove by heating in an oven at 800 K [12], and these organic compounds can be assumed to also evaporate during laser heating. Bambha et al. experimentally showed the significant influence of a non-absorbing coating (oleic acid) on the fluence curve of mature soot [55], where corresponding amount of coating mass fraction yielded a fluence curve shift of 0.020 and 0.070 J/cm^2 for 20 and 86% coating mass fraction,

respectively. Assuming that the evaporated species of the OP6 and OP7 soot has comparable thermal properties to that of oleic acid, a shift of 0.09 and 0.25 J/cm^2 at 1064 nm could be expected for OP6 and OP7 soot. This would however not result in any major influence on the $E(m, \lambda)$ estimations, see section S4 in supplemental information.

It should be kept in mind that in our work, we consider the influence of non-refractory PAH and organics condensed on, and/or partially mixed with young soot, as the soot itself is a polydisperse distribution consisting of a variety of sizes and levels of maturity. Thereby the core–shell analogy does not necessarily describe our types of immature soot. Furthermore, it was observed in [12] that the evaporation of PAHs and organics induced a change in the wavelength-dependent absorption properties as the dispersion coefficient ξ decreased from 3.5 to 2.5 for OP7, indicating that the evaporated species were absorbing, at least at shorter wavelengths. Hence, it could be argued that a potential fluence curve shift due to evaporation of volatiles may be smaller at excitation wavelengths of 532 nm and thereby our ξ estimations for OP6 and OP7 might even be somewhat over-estimated.

5 Conclusions

LII fluence curves have been measured for different types of cold soot (from young to mature) to retrieve information about their absorption properties. By the use of two excitation wavelengths and by detecting the LII signal at two wavelength bands, (1) the wavelength-dependent absorption properties, (2) the LIF contribution when using 532 nm excitation wavelength, and (3) the $E(m, \lambda)$-trends could be observed. The main findings are the following:

- Fluence curve analysis at 532 nm was made on the LII signal after a delay of 50 ns after the peak LII signal to avoid LIF interference from fluorescing species. These fluence curves could then be used to estimate the dispersion coefficient of the studied soot. Good agreement for the mature soot was observed with values obtained using multi-wavelength extinction in a previous study. For the less mature soot, however, the LII-derived dispersion coefficients appeared lower, and it is therefore speculated that thermal annealing may at least partly be responsible for the lowering as the soot may become more ordered during rapid heating.
- The fluence curves at delay 50 ns were also used to estimate the influence of LIF depending on detection wavelength when using $\lambda_{laser} = 532$ nm. The largest contribution was detected using 575 nm detection wavelength; however, an apparent contribution was also observed at 684 nm.

- The absorption efficiency of the mature OP1 soot was investigated by observing the temperature evolution of laser-heated soot in the low-fluence regime. It was estimated that $E(m, 1064$ nm$)$ is 0.33 for OP1 soot, which agrees well with the values presented in the literature. The LII model was used to obtain $E(m, 1064$ nm$)$ for the young soot types, resulting in values of 0.16 and 0.05 for OP6 and OP7 soot, respectively. An uncertainty analysis was conducted to investigate how the material parameters used for the less mature soot might add uncertainties to our estimated $E(m, \lambda)$ values. It was shown that simulations using our LII model could not show any significant influence by parameter variation. The influence of absorbing organic coatings is discussed and initial estimations indicated a relatively small impact on the estimated $E(m, \lambda)$.

Furthermore, the wide spread of $E(m, \lambda)$ for soot of different maturity suggests important aspects of experimental work when performing quantitative soot measurements using a laser wavelength of 1064 nm. As the choice of operating fluence often is selected based on the absorption properties of mature soot, young soot particles with lower $E(m)$ might not be sufficiently heated to reach the fluence in-sensitive plateau, or to give any significant LII signal contribution at all.

References

1. H. Wang, Proc. Combust. Inst. **33**(1), 41–67 (2011)
2. H. Bockhorn, *Soot Formation in Combustion: Mechanisms and Models*, vol. 59 (Springer Science and Business Media, 2013).
3. H.A. Michelsen, M.B. Colket, P.-E. Bengtsson, A. D'Anna, P. Desgroux, B.S. Haynes, J.H. Miller, G.J. Nathan, H. Pitsch, H. Wang, ACS Nano. (2020)
4. N.-E. Olofsson, J. Simonsson, S. Török, H. Bladh, P.-E. Bengtsson, Appl. Phys. B **119**(4), 669–683 (2015)
5. X. López-Yglesias, P.E. Schrader, H.A. Michelsen, J. Aerosol Sci. **75**, 43–64 (2014)
6. K.O. Johansson, F. El Gabaly, P.E. Schrader, M.F. Campbell, H.A. Michelsen, Aerosol Sci. Technol. **51**(12), 1333–1344 (2017)
7. F. Migliorini, K.A. Thomson, G.J. Smallwood, Appl. Phys. B Lasers Opt. **104**(2), 273–283 (2011)
8. J. Simonsson, N.-E. Olofsson, S. Török, P.-E. Bengtsson, H. Bladh, Appl. Phys. B **119**(4), 657–667 (2015)
9. S. Maffi, S. De Iuliis, F. Cignoli, G. Zizak, Appl. Phys. B **104**(2), 357–366 (2011)
10. IPCC, *Climate Change 2013: The Physical Science Basis. Contribution of Working Group I to the Fifth Assessment Report of the Intergovernmental Panel on Climate Change* (Cambridge University Press, Cambridge and New York, 2013), p. 1535
11. T.C. Bond, S.J. Doherty, D.W. Fahey, P.M. Forster, T. Berntsen, B.J. DeAngelo, M.G. Flanner, S. Ghan, B. Kärcher, D. Koch, S. Kinne, Y. Kondo, P.K. Quinn, M.C. Sarofim, M.G. Schultz, M. Schulz, C. Venkataraman, H. Zhang, S. Zhang, N. Bellouin, S.K. Guttikunda, P.K. Hopke, M.Z. Jacobson, J.W. Kaiser, Z. Klimont, U. Lohmann, J.P. Schwarz, D. Shindell, T. Storelvmo, S.G. Warren, C.S. Zender, J. Geophys. Res. Atmos. **118**(11), 5380–5552 (2013)
12. S. Török, V.B. Malmborg, J. Simonsson, A. Eriksson, J. Martinsson, M. Mannazhi, J. Pagels, P.-E. Bengtsson, Aerosol Sci. Technol. **52**(7), 757–767 (2018)
13. H. Bladh, J. Johnsson, N.-E. Olofsson, A. Bohlin, P.-E. Bengtsson, Proc. Combust. Inst. **33**(1), 641–648 (2011)
14. G. Cléon, T. Amodeo, A. Faccinetto, P. Desgroux, Appl. Phys. B Lasers Opt. **104**(2), 297–305 (2011)
15. H.A. Michelsen, C. Schulz, G.J. Smallwood, S. Will, Prog. Energy Combust. Sci. **51**, 2–48 (2015)
16. F. Liu, J. Yon, A. Fuentes, P. Lobo, G.J. Smallwood, J.C. Corbin, Aerosol Sci. Technol. **54**(1), 33–51 (2020)
17. A. Bescond, J. Yon, F.-X. Ouf, C. Rozé, A. Coppalle, P. Parent, D. Ferry, C. Laffon, J. Aerosol Sci. **101**, 118–132 (2016)
18. R.H. Moore, L.D. Ziemba, D. Dutcher, A.J. Beyersdorf, K. Chan, S. Crumeyrolle, T.M. Raymond, K.L. Thornhill, E.L. Winstead, B.E. Anderson, Aerosol Sci. Technol. **48**(5), 467–479 (2014)
19. M.N. Ess, K. Vasilatou, Aerosol Sci. Technol. **53**(1), 29–44 (2019)
20. M.M. Maricq, Aerosol Sci. Technol. **48**(6), 620–629 (2014)
21. L. Durdina, P. Lobo, M.B. Trueblood, E.A. Black, S. Achterberg, D.E. Hagen, B.T. Brem, J. Wang, Aerosol Sci. Technol. **50**, 906–918 (2016)
22. M. Saffaripour, L.-L. Tay, K.A. Thomson, G.J. Smallwood, B.T. Brem, L. Durdina, M. Johnson, Aerosol Sci. Technol. **51**(4), 518–531 (2017)
23. A. Mamakos, I. Khalek, R. Giannelli, M. Spears, Aerosol Sci. Technol. **47**(8), 927–936 (2013)
24. V.B. Malmborg, A.C. Eriksson, S. Török, Y. Zhang, K. Kling, J. Martinsson, E.C. Fortner, L. Gren, S. Kook, T.B. Onasch, Carbon **142**, 535–546 (2019)
25. K.C. Le, T. Pino, J. Henriksson, S. Török, P.-E. Bengtsson, Combust. Flame **209**, 291–302 (2019)
26. I. Marhaba, D. Ferry, C. Laffon, T.Z. Regier, F.-X. Ouf, P. Parent, Combust. Flame **204**, 278–289 (2019)
27. H.A. Michelsen, Proc. Combust. Inst. **36**(1), 717–735 (2017)
28. E. Therssen, Y. Bouvier, C. Schoemaecker-Moreau, X. Mercier, P. Desgroux, M. Ziskind, C. Focsa, Appl. Phys. B **89**(2), 417–427 (2007)
29. S. Bejaoui, R. Lemaire, P. Desgroux, E. Therssen, Appl. Phys. B **116**(2), 313–323 (2014)

30. T. Sipkens, K. Daun, Opt. Express **25**(5), 5684–5696 (2017)
31. S. De Iuliis, F. Migliorini, F. Cignoli, G. Zizak, Appl. Phys. B **83**(3), 397 (2006)
32. C. Schulz, B.F. Kock, M. Hofmann, H. Michelsen, S. Will, B. Bougie, R. Suntz, G. Smallwood, Appl. Phys. B **83**(3), 333 (2006)
33. H. Bladh, J. Johnsson, P.-E. Bengtsson, Appl. Phys. B **90**(1), 109–125 (2008)
34. H. Michelsen, F. Liu, B.F. Kock, H. Bladh, A. Boïarciuc, M. Charwath, T. Dreier, R. Hadef, M. Hofmann, J. Reimann, Appl. Phys. B **87**(3), 503–521 (2007)
35. Jing. *Mini-CAST soot generator*. 2009 [cited 2019 October]. Available from: http://www.sootgenerator.com/.
36. V.B. Malmborg, A.C. Eriksson, S. Török, Y. Zhang, K. Kling, J. Martinsson, E.C. Fortner, L. Gren, S. Kook, T.B. Onasch, P.-E. Bengtsson, J. Pagels, Carbon **142**, 535–546 (2019)
37. N.-E. Olofsson, J. Johnsson, H. Bladh, P.-E. Bengtsson, Appl. Phys. B Lasers Opt. **112**(3), 333–342 (2013)
38. F. Migliorini, S. De Iuliis, S. Maffi, G. Zizak, Appl. Phys. B **120**(3), 417–427 (2015)
39. S. Bejaoui, X. Mercier, P. Desgroux, E. Therssen, Combust. Flame **161**(10), 2479–2491 (2014)
40. A. Ångström, Geogr. Ann. **11**, 156–166 (1929)
41. R.L. Vander Wal, M.Y. Choi, Carbon **37**(2), 231–239 (1999)
42. R.L. Vander Wal, T. Ticich, A. Stephens, Appl. Phys. B **67**(1), 115–123 (1998)
43. M. Saffaripour, K.-P. Geigle, D.R. Snelling, G.J. Smallwood, K.A. Thomson, Appl. Phys. B **119**(4), 621–642 (2015)
44. K. Thomson, K. Geigle, M. Köhler, G. Smallwood, D. Snelling, Appl. Phys. B **104**(2), 307–319 (2011)
45. F. Migliorini, S. De Iuliis, R. Dondè, M. Commodo, P. Minutolo, A. D'Anna, Exp. Thermal Fluid Sci. **114**, 110064 (2020)
46. K. Wan, X. Shi, H. Wang, Proc. Combust. Inst. **38**(1), 1517–1524 (2021)
47. H.A. Michelsen, A.V. Tivanski, M.K. Gilles, L.H. van Poppel, M.A. Dansson, P.R. Buseck, Appl. Opt. **46**(6), 959–977 (2007)
48. H.A. Michelsen, Proc. Combust. Inst. **38**(1), 1197–1205 (2021)
49. H. Bladh, P.-E. Bengtsson, J. Delhay, Y. Bouvier, E. Therssen, P. Desgroux, Appl. Phys. B **83**(3), 423–433 (2006)
50. J. Johnsson, H. Bladh, N.-E. Olofsson, P.-E. Bengtsson, Appl. Phys. B **112**(3), 321–332 (2013)
51. F. Goulay, L. Nemes, P.E. Schrader, H.A. Michelsen, Mol. Phys. **108**(7–9), 1013–1025 (2010)
52. S.M. Musikhin, R.; Smallwood, G. J.; Dreier, T.; Daun, K. J.; Schulz, C., In Proceedings of Combustion Institute–Canadian Section (2019)
53. P.-E. Bengtsson, M. Aldén, Appl. Phys. B **60**(1), 51–59 (1995)
54. J.P. Abrahamson, M. Singh, J.P. Mathews, R.L. Vander Wal, Carbon **124**, 380–390 (2017)
55. R.P. Bambha, M.A. Dansson, P.E. Schrader, H.A. Michelsen, Appl. Phys. B **112**(3), 343–358 (2013)